physics

MDPI

Article

Finite-Capacity Spacetime and Entropic Contributions to Cosmological Structure Formation

Florian Neukart [1,2,*], Eike Marx [2] and Valerii Vinokur [2,†]

[1] Leiden Institute of Advanced Computer Science, Leiden University, Gorlaeus Gebouw-BE-Vleugel, Einsteinweg 55, 2333 Leiden, The Netherlands
[2] Terra Quantum AG, Kornhausstrasse 25, 9000 St. Gallen, Switzerland; eike@terraquantum.swiss (E.M.)
* Correspondence: f.neukart@liacs.leidenuniv.nl
† Deceased author.

Abstract

We investigatewhether a finite local information capacity of spacetime can account for the gravitational phenomena commonly attributed to cold dark matter. Starting from a covariant effective-field-theory description, we modelcoarse-grained entropy deposition as a dynamical scalar field $S(x)$ whose stress–energy tensor contributes to structure formation. The macroscopic action contains a single dimensionless coupling λ multiplying the canonical kinetic term, ensuring ghost-free dynamics and conservation of the associated stress–energy tensor. In a slow-roll regime, defined by a covariant source term $\Gamma \equiv \ddot{S} + 3H\dot{S} = 0$, where H is the Hubble parameter and overdot denotes derivative with respect to cosmic time, and $|\ddot{S}| \ll H|\dot{S}|$, the entropy sector behaves as pressureless dust at background and in linear order. Implemented in a modified Cosmic Linear Anisotropy Solving System (CLASS) Boltzmann solver, the entropy component fits Planck satellite 2018 cosmic microwave background (CMB) data, baryon acoustic oscillation (BAO) measurements, and the Pantheon + Type Ia supernova sample for $0.5 \lesssim \lambda \lesssim 2$, while preserving the linear growth factor to within 0.2% over Euclid space telescope scales. To regulate ultraviolet contributions, we introduce a holographically motivated prescription in which gravitationally active entropy deposition is confined to causal two-surfaces, yielding a $\rho \propto r^{-2}$ halo envelope with a finite-density core determined by local entropy saturation. Fixing the flux scale $\mathcal{A}$ from astrophysical entropy budgets reproduces Milky-Way-mass halos without introducing fine-tuned length scales. Pilot N-body simulations that evolve the entropy field on a staggered grid reproduce the halo mass function down to $10^{10.5}\,M_{\odot}$, mitigate the cusp–core and missing-satellite tensions, and remain consistent with cluster lensing constraints. On linear scales, the model predicts percent-level, scale-dependent deviations in the lensing convergence and matter power spectra, testable by Euclid space telescope, the Roman Space Telescope High Latitude Survey, and the CMB-S4 experiment.

Keywords: quantum information; effective field theory; dark matter phenomenology; dark matter alternatives; emergent gravity; coarse-grained entropy field; galaxy rotation curves; weak gravitational lensing; large-scale structure; CMB anisotropies; N-body simulations; cosmological perturbation theory

Received: 1 April 2026
Accepted: 30 April 2026
Published: 2 June 2026

1. Introduction

The first indications that the visible mass in galaxies is insufficient to account for their observed kinematics date back to the pioneering study by Vera Rubin and W. Kent

Ford, who showed that spiral-galaxy rotation curves remain flat well beyond the luminous disk [1]. On cosmological scales, the ΛCDM model reproduces the acoustic peaks of the cosmic microwave background (CMB) and the baryon–acoustic oscillation (BAO) standard ruler with a high precision [2,3], while N-body simulations successfully describe the large-scale distribution of matter and the halo mass function [4]. These results provide strong evidence for a non-luminous component that dominates the gravitational dynamics of the Universe. At the same time, several persistent discrepancies at the galactic and sub-galactic scales continue to motivate further investigation of the dark sector. Dwarf galaxies often exhibit slowly rising inner density profiles that are less steep than those predicted by collisionless simulations; satellite counts around the Milky Way are lower than expected from subhalo statistics; and the most massive satellites appear difficult to reconcile with standard concentration–mass relations [5]. At cluster scales, the Bullet Cluster demonstrates a clear separation between baryonic gas and the gravitational potential inferred from weak lensing [6]. More recently, weak-lensing measurements from Euclid space telescope have indicated possible mild scale-dependent deviations in the convergence power spectrum, although the current uncertainties remain significant [7]. While none of these observations individually require a departure from ΛCDM, taken together, they motivate exploring alternative or complementary descriptions of the dark sector. A long-standing line of research suggests that gravitational dynamics may encode thermodynamic or informational properties of microscopic degrees of freedom. The identification of a black-hole horizon area with entropy by Jacob D. Bekenstein, together with Stephen Hawking's derivation of black-hole radiation, established a quantitative link between geometry and information [8]. Ted Jacobson subsequently showed that the Einstein field equations can be interpreted as an equation of state arising from the local entropy balance across causal horizons [9]. More recent approaches have explored the possibility that galactic dynamics and lensing may emerge from coarse-grained information or entanglement structure [10–12]. These perspectives suggest that gravitational phenomena traditionally attributed to dark matter may, at least in part, reflect collective properties of underlying microscopic degrees of freedom. However, existing approaches of this type typically do not provide a single framework that simultaneously reproduces precision cosmology, linear perturbation growth, and nonlinear structure formation within a controlled and testable effective theory [13,14]. This motivates the development of a formulation in which information-theoretic effects enter gravitational dynamics through an additional macroscopic sector that remains consistent with general relativity and can be confronted with observational data across multiple scales.

In this paper, we introduce a scalar field $S(x)$ that represents a coarse-grained measure of microscopic entropy production per spacetime region. The field $S(x)$ is not interpreted as a fundamental particle-physics scalar. Rather, it is an effective infrared variable obtained by coarse-graining over microscopic degrees of freedom associated with finite-capacity spacetime regions. Its role is therefore analogous to hydrodynamic variables such as density or temperature, encoding the collective behavior of many underlying degrees of freedom rather than introducing a new fundamental field. This interpretation is illustrated schematically in Figure 1, where spacetime is represented as a collection of finite-capacity regions that store local information, and astrophysical processes induce localized entropy updates. The coarse-grained field $S(x)$ encodes the cumulative effect of such microscopic information processing.

https://doi.org/10.3390/physics8020049

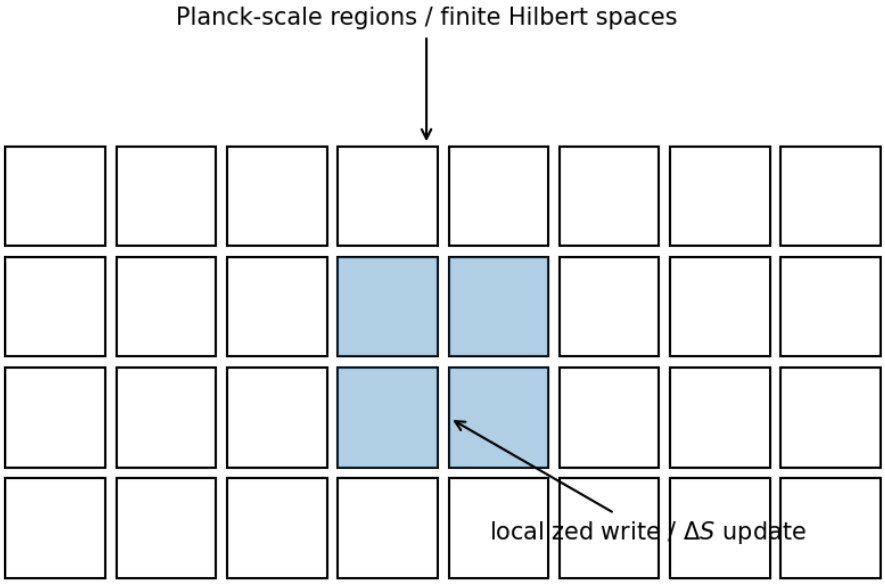

Figure 1. Schematic illustration of finite-capacity spacetime regions and localized entropy updates. The coarse-grained field $S(x)$ represents accumulated microscopic information stored across such regions.

The central assumption of this framework is that coarse-grained entropy production can be mapped to an effective stress–energy contribution that is covariantly conserved at macroscopic scales. Unlike entirely phenomenological modifications of gravity, this contribution is derived from a variational principle at the level of the effective theory, ensuring consistency with general relativity while allowing for additional contributions arising from coarse-grained microscopic dynamics. We consider an infrared effective description in which the entropy field contributes through a local, covariant action whose leading operator is the canonical gradient term $(\partial S)^2$. Higher-order operators are suppressed at large scales in a derivative expansion. The distinction from standard scalar-field cosmology lies not in the structure of the action, but in the interpretation and sourcing of the field: $S(x)$ encodes the accumulated entropy production associated with coarse-grained microscopic processes, rather than representing a fundamental dynamical degree of freedom with an independent potential. A key aspect of the framework is the coexistence of two complementary descriptions with distinct domains of validity. On large, approximately homogeneous scales, the entropy field evolves according to the effective action and contributes to cosmological expansion and perturbations. On smaller, nonlinear scales, where coarse-graining over microscopic degrees of freedom leads to localized entropy deposition, an effective causal-surface description becomes more appropriate. In this description, gravitationally active entropy is associated with effective causal boundaries, leading to halo profiles with finite cores and extended envelopes. The relation between these two descriptions is not a strict derivation from a single local field equation, but rather a consistent coarse-grained mapping between the microscopic entropy flux and the macroscopic gravitational response, which we make explicit in Sections 3–8. A possible microscopic realization of this picture is provided by the quantum memory matrix (QMM) [15–18], in which spacetime consists of finite-dimensional Hilbert spaces associated with Planck-scale regions that store and update quantum information. The results presented here, however, rely only on the infrared effective description and do not depend on the specific details of the ultraviolet completion. This separation allows the framework to be tested observationally without committing to a particular microscopic model. This paper develops a quantitative and testable cosmological model in which the entropy sector contributes to structure formation across multiple scales. We focus on observables that allow for a direct

comparison with ΛCDM, including the CMB temperature, polarization, and lensing residuals; large-scale structure statistics; and galaxy rotation curves. Relative to earlier exploratory studies, this paper presents a joint study of entropy-sector parameters across cosmological and galactic datasets, introduces a causal-surface-based halo model validated against rotation-curve observations, and incorporates the entropy field into structure-formation simulations. The remainder of the paper is organized as follows. Section 2 derives the effective action and corresponding stress–energy tensor. Section 3 introduces the causal-surface description and its connection to the field-theoretic formulation. Section 5 analyzes the background cosmology, while Sections 6 and 7 present the linear and nonlinear structure formation. Section 8 discusses galactic and cluster-scale observables, and Section 9 examines the stability and consistency conditions.

Throughout, we employ natural units $c = \hbar = 1$, where c denotes the speed of light and $\hbar$ is the reduced Planck constant, and a metric signature $(-,+,+,+)$.

2. Microscopic Foundations of the Entropy Field

We begin by specifying a microscopic picture that motivates the introduction of a coarse-grained entropy field while remaining agnostic about the exact ultraviolet completion. The working assumption is that spacetime admits a finite local information capacity, consistent with holographic bounds and causal-set-inspired constructions [19–21]. This assumption provides a natural regulator of ultraviolet degrees of freedom while preserving locality and compatibility with diffeomorphism invariance at macroscopic scales. At the microscopic level, we consider spacetime as composed of Planck-scale four-volumes, each associated with a finite-dimensional Hilbert space $\mathcal{H}_i$. Local quantum interactions update the reduced density operator of fields restricted to each region via unitary maps

$$\rho_i \;\mapsto\; U_i\,\rho_i\,U_i^{\dagger},$$

where ρ_i denotes the reduced density matrix of all fields in region i. Because the number of accessible microstates is finite, this construction implements a finite information capacity per spacetime region without introducing a preferred frame or violating locality at macroscopic scales. The entropy associated with each region is given by the von Neumann entropy

$$S_i \equiv -\,\mathrm{Tr}(\rho_i \log \rho_i),$$

which is a scalar quantity under coordinate transformations. For macroscopic regions containing many such elements, we define a coarse-grained entropy field

$$S(x) = \frac{1}{N_\Omega} \sum_{i \in \Omega} S_i, \tag{1}$$

where Ω is a coarse-graining domain containing $N_\Omega \gg 1$ microscopic regions. This construction is analogous to the emergence of thermodynamic variables from microscopic degrees of freedom. In particular, $S(x)$ does not represent an additional fundamental field, but rather an effective infrared variable encoding collective information associated with many microscopic degrees of freedom. A schematic representation of this coarse-graining procedure is shown in Figure 1. To obtain macroscopic dynamics, we performed real-space coarse-graining in which degrees of freedom below a characteristic scale $L \gg l_{\mathrm{Pl}}$, where l_{Pl} is the Planck length, are integrated out. The resulting infrared description is expressed in terms of a smooth scalar field $S(x)$ defined over spacetime. By construction, this field inherits locality and covariance from the underlying microscopic theory. The effective action must therefore be local, diffeomorphism invariant, and constructed from scalar operators involving $S(x)$ and the metric.

https://doi.org/10.3390/physics8020049

To the leading order in a derivative expansion, the most general action consistent with these requirements is

$$\mathcal{S}_{\text{eff}}[S, g] = \int d^4x \sqrt{-g} \left[\frac{\lambda}{2} g^{\mu\nu} \partial_\mu S \partial_\nu S + \mathcal{O}\left(\frac{l_{\text{Pl}}^2}{L^2} \right) \right]. \tag{2}$$

Here, $g_{\mu\nu}$ is the metric tensor with the Greek indices taking the values 0 for the temporal component and 1, 2, and 3 for the space components; $\partial_\nu = \partial/\partial x^\nu$ denotes coordinate differentiation.

This structure follows from standard effective field theory arguments. Locality and covariance restrict the operator basis, while a dimensional calculation implies that higher-order operators are suppressed by powers of l_{Pl}/L. Subleading contributions include operators such as $(\partial S)^4$, curvature couplings, and nonlocal terms generated by integrating out microscopic degrees of freedom. Their contributions are parametrically suppressed in the regime $L \gg l_{\text{Pl}}$, ensuring that the truncation to Equation (2) is controlled and systematically improvable. Importantly, no potential term $V(S)$ appears at the leading order. This reflects the feature that $S(x)$ represents accumulated entropy production rather than a fundamental scalar with an independent vacuum expectation value. Any effective potential arises only at the subleading order through coarse-graining and would be suppressed relative to the kinetic term in the infrared regime considered here. Variation in the action with respect to the metric yields the stress–energy tensor

$$T_{\mu\nu}^{(S)} = \lambda \left(\partial_\mu S \, \partial_\nu S - \frac{1}{2} g_{\mu\nu} (\partial S)^2 \right), \tag{3}$$

which is uniquely determined and covariantly conserved as a consequence of diffeomorphism invariance. This ensures that the entropy contribution to the Einstein equations follows directly from a variational principle and is not introduced phenomenologically. At the level of Equation (2), the structure is formally equivalent to that of a minimally coupled scalar field with vanishing potential. In conventional cosmology, such a field corresponds to a stiff fluid with an equation of state $w = 1$, typically leading to rapidly decelerating expansion. In the present framework, however, this identification is incomplete. The key difference lies in the interpretation and sourcing of the field. The variable $S(x)$ does not describe an independent microscopic degree of freedom, but a coarse-grained quantity encoding accumulated entropy production associated with underlying microscopic processes. As a result, its spatial distribution and temporal evolution are not arbitrary, but constrained by the underlying information flow and causal structure. In particular, configurations relevant for cosmology are generically inhomogeneous and dynamically sourced, leading after coarse-graining to effective behavior that differs from that of a homogeneous stiff fluid. This distinction becomes essential when connecting the field description to nonlinear structure formation. On sufficiently large scales, effective field theory provides a valid description of the dynamics of $S(x)$. On smaller scales, where entropy production becomes localized and strongly inhomogeneous, a complementary coarse-grained description in terms of entropy flux across effective causal surfaces becomes more appropriate. The relation between these two descriptions is not a direct derivation from a single local field equation, but a consistent mapping between microscopic entropy flow and a macroscopic gravitational response, which we develop explicitly in Section 3. The dimensionless coupling λ encodes the efficiency with which entropy gradients contribute to the effective stress–energy tensor. As the operator $(\partial S)^2$ is marginal in four dimensions, λ is technically natural and expected to be of order unity, with at most logarithmic running under renormalization. Its value

is therefore determined phenomenologically through comparison with cosmological and astrophysical data.

Starting from a finite-capacity microscopic picture, we obtain a coarse-grained entropy field whose dynamics follow from a well-defined variational principle. The resulting stress–energy tensor is uniquely determined and covariantly conserved, and the effective theory is controlled by a single dimensionless parameter λ. These results establish the theoretical consistency of the framework and provide the foundation for the cosmological and astrophysical investigation that follows.

3. Holographically Regulated Entropic Deposition

The effective field theory introduced in Section 2 specifies how the coarse-grained entropy field contributes to gravity through a well-defined variational principle. What remains is to determine how microscopic entropy production is mapped onto macroscopic gravitational sourcing in realistic astrophysical environments. A spatially homogeneous entropy field does not reproduce the observed localization of gravitational mass in halos and clusters. The missing ingredient is a physically motivated mechanism that determines which entropy contributions survive coarse-graining and remain gravitationally active. We identify this mechanism with irreversible information transfer across dynamically emergent causal boundaries. Only entropy associated with processes that cannot be reversed within the local causal domain contributes to the macroscopic entropy field. We refer to this mechanism as holographically regulated entropic deposition (HRED). These effective causal surfaces arise generically in nonlinear gravitational systems. Examples include virialization fronts, radiative cooling boundaries, and decoherence layers in strongly interacting environments. Their defining property is that information transfer across them becomes effectively irreversible, preventing re-localization of microscopic correlations. Entropy production that remains locally reversible does not contribute to long-range gravitational sourcing, while entropy crossing such surfaces is retained in the coarse-grained description.

3.1. Entropy Flux Across Causal Surfaces

Consider a virialized halo of radius R. The outermost causal enclosure defines an effective causal surface (ECS) that separates the interior from the surrounding environment. Entropy production associated with irreversible processes inside the halo is transported across this surface. Locality, isotropy, and dimensional analyses constrain the leading-order contribution to the entropy flux to scale with the surface area:

$$\frac{dS}{dt} = 4\pi R^2 \mathcal{A}, \tag{4}$$

where $\mathcal{A}$ is an entropy-flux coefficient encoding the efficiency of irreversible information transfer. This scaling follows from the feature that entropy transport occurs through local interactions across a boundary of codimension one. Higher-order corrections involving curvature or nonlocal effects are suppressed by powers of R^{-1} or $(l_{\rm Pl}/R)^2$, and are therefore negligible on galactic and cluster scales. Integrating Equation (4) over a characteristic timescale yields the cumulative entropy associated with the causal surface,

$$S(R) = 4\pi \mathcal{A} R^2 t_{\rm eff}, \tag{5}$$

where $t_{\rm eff}$ is the effective duration over which entropy accumulation remains active. For virialized systems, $t_{\rm eff}$ is naturally of the order of the Hubble time t_H, reflecting the long-lived nature of halo structures.

3.2. Mapping Entropy to Gravitational Mass

To relate entropy to gravitational sourcing, we interpret irreversible entropy production as carrying an effective energy scale set by the typical temperature of dissipative processes. This leads to the relation

$$E = k_{\mathrm{B}} T_{\mathrm{eff}}\, S, \tag{6}$$

where T_{eff} represents an effective temperature characterizing processes such as shocks, stellar feedback, and radiative cooling, and k_{B} is the Boltzmann constant. The adopted physical bounds on this effective temperature and their impact on the calibration are given in Appendix A. The corresponding gravitationally active mass is then

$$M_{\mathrm{S}}(R) = \frac{4\pi\, \mathcal{A}\, k_{\mathrm{B}} T_{\mathrm{eff}}\, t_{\mathrm{eff}}}{c^2}\, R^2 \;\equiv\; \eta\, R^2, \tag{7}$$

where η is an effective proportionality constant determined by microscopic entropy production rates and macroscopic energy scales. The quadratic scaling arises directly from the area law in Equation (4) and does not rely on assumptions about particle dark matter or modifications of gravity.

3.3. Finite-Capacity Saturation

The finite information capacity introduced in Section 2 implies that entropy accumulation cannot proceed indefinitely. Once the available coarse-grained capacity is saturated, additional microscopic entropy production does not increase the macroscopic entropy field. We therefore introduce a saturation scale R_s, defined as the radius at which entropy deposition transitions from an accumulation regime to a capacity-limited regime. Beyond this scale, entropy production no longer increases the effective field, and the cumulative mass grows more slowly. To model this transition without introducing discontinuities, we employ a smooth interpolation that preserves the asymptotic limits,

$$M_{\mathrm{S}}(R) = \eta R^2 \left(1 + \frac{R}{R_s}\right)^{-1} + \eta R_s R \left(1 + \frac{R_s}{R}\right)^{-1}. \tag{8}$$

This expression yields the limiting behavior

$$M_{\mathrm{S}}(R) \propto \begin{cases} R^2, & R \ll R_s, \\ R, & R \gg R_s, \end{cases}$$

corresponding to a transition from entropy-dominated growth to capacity-limited scaling. The associated density profile is

$$\rho_{\mathrm{S}}(r) \propto \begin{cases} r^{-1}, & r \ll R_s, \\ r^{-2}, & r \gg R_s, \end{cases}$$

which is consistent with observed halo structures across galactic-to-cluster scales.

3.4. Resulting Halo Structure

The resulting cumulative mass profile is shown in Figure 2.

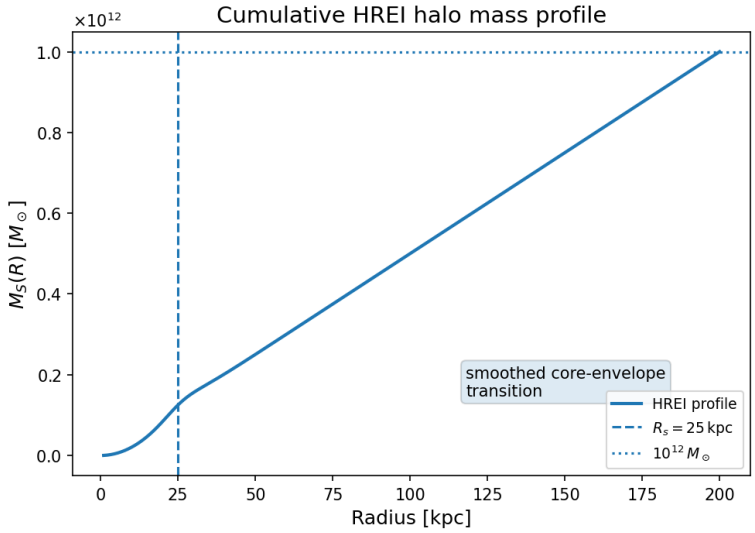

Figure 2. Cumulative halo mass profile resulting from holographically regulated entropic deposition. The transition at R_s separates an unsaturated regime with $M \propto R^2$ from a capacity-limited regime with $M \propto R$, corresponding to a smooth transition from an inner r^{-1} profile to an outer r^{-2} envelope. The abscissa shows the halo radius R in kiloparsecs, the ordinate shows the cumulative entropy-sector mass $M_S(R)$ in solar masses, the vertical dashed line marks the saturation radius R_s, and the horizontal dotted reference line marks $10^{12} M_\odot$.

This behavior reproduces key observational features of galactic halos. The inner scaling generates approximately flat rotation curves, while the outer scaling is consistent with weak-lensing measurements and cluster mass profiles.

3.5. Parameter Estimates and Observational Scale

The entropy-flux coefficient $\mathcal{A}$ can be estimated from global entropy production processes, including stellar evolution, supernova feedback, and active galactic nuclei. These considerations yield

$$\mathcal{A} \approx (10^{25}\text{–}10^{26})\,\mathrm{J\,K^{-1}\,s^{-1}\,m^{-2}},$$

which leads to characteristic halo masses of order $10^{12} M_\odot$ at $R \approx 200\,\mathrm{kpc}$, consistent with Milky-Way-scale systems without requiring direct fitting to rotation curves. The astrophysical entropy-production estimate and dominant calibration systematics are summarized in Appendix B.

3.6. Connection to Cosmology

At cosmological scales, the same mechanism leads to a scale-dependent contribution to the matter distribution. The entropy sector behaves as an additional non-baryonic component whose spatial distribution reflects the history of irreversible processes rather than particle dynamics. This produces percent-level deviations in matter clustering and lensing at intermediate scales, while the saturation mechanism suppresses excessive growth at late times, maintaining consistency with CMB and BAO observations [2,3].

Holographically regulated entropic deposition provides the link between the effective field theory of Section 2 and observable structure formation. It specifies how microscopic entropy production is converted into a macroscopic gravitational source, yielding a unified description of the halo structure and cosmological evolution without introducing new particle species or modifying the Einstein equations.

4. Effective Action and Field Equations

We now construct the macroscopic description governing the gravitational response of the coarse-grained entropy sector introduced in Section 2. A central requirement is that all field equations follow from a variational principle at the level of the effective theory, ensuring covariance, conservation, and internal consistency. The infrared action combining general relativity, Standard Model matter, and the entropy field is

$$\mathcal{S} = \frac{1}{16\pi G}\int d^4x\,\sqrt{-g}\,\mathcal{R} + \int d^4x\,\sqrt{-g}\,\mathcal{L}_{\rm SM} + \frac{\lambda}{16\pi G}\int d^4x\,\sqrt{-g}\,(\nabla_\mu S)(\nabla^\mu S), \quad (9)$$

where G is Newton's gravitational constant, g is the determinant of the metric tensor, $\mathcal{R}$ is the Ricci scalar. The structure of Equation (9) coincides formally with that of a minimally coupled scalar field with vanishing potential. The coarse-grained path-integral derivation motivating this effective action is summarized in Appendix C. However, as emphasized below, the physical interpretation and sourcing of $S(x)$ differ fundamentally from standard scalar-field models.

4.1. Variation and Stress–Energy Tensor

The macroscopic dynamics of the entropy sector are derived from the effective action introduced in Equation (9). Varying the total action with respect to the metric yields the modified Einstein equations

$$G_{\mu\nu} = 8\pi G\left(T^{(\rm SM)}_{\mu\nu} + T^{(S)}_{\mu\nu}\right), \quad (10)$$

where $G_{\mu\nu}$ is the Einstein tensor and the entropy-sector contribution is obtained directly from functional differentiation,

$$T^{(S)}_{\mu\nu} = -\frac{2}{\sqrt{-g}}\frac{\delta S_{\rm eff}}{\delta g^{\mu\nu}} = \lambda\left(\nabla_\mu S\,\nabla_\nu S - \frac{1}{2}g_{\mu\nu}(\nabla S)^2\right). \quad (11)$$

Thus, the stress–energy tensor is not postulated, but follows uniquely from the variational principle. By construction, it satisfies

$$\nabla^\mu T^{(S)}_{\mu\nu} = 0 \quad (12)$$

when the entropy field obeys its equation of motion, ensuring compatibility with the Bianchi identity and the overall consistency of the gravitational field equations. This point is essential: the entropy sector is introduced at the level of the action, not at the level of the field equations. Consequently, all gravitational dynamics follow from a single covariant variational framework, and no phenomenological insertion of an energy–momentum tensor is required.

4.2. Equation of Motion and Open-System Interpretation

Variation in the effective action with respect to the entropy field S yields the Euler–Lagrange equation:

$$\Box S = 0, \quad (13)$$

which defines the fundamental, closed-system dynamics of the coarse-grained field within the effective theory.

However, the entropy field does not represent an isolated microscopic degree of freedom. Instead, it arises from coarse-graining over underlying quantum and statistical processes that continuously generate entropy through irreversible interactions. As a result, the physically realized macroscopic dynamics correspond to an open system. A systematic derivation of this behavior can be obtained by integrating out microscopic degrees of

freedom using an influence-functional or coarse-grained effective-action formalism. At the level of expectation values, this leads to an effective equation of motion of the form

$$\Box S = \Gamma, \tag{14}$$

where $\Gamma(x)$ is a covariant source term encoding the coarse-grained entropy-production rate.

Importantly, Equation (14) does not modify the underlying action, and therefore, does not alter the variational origin of the theory. Instead, it represents the effective, macroscopic evolution equation after integrating out unresolved microscopic degrees of freedom, in direct analogy with nonequilibrium effective field theories. Consistency with general covariance is maintained as follows. The total stress–energy tensor, including both the entropy sector and the integrated-out microscopic contributions, remains conserved:

$$\nabla^\mu \left(T^{(S)}_{\mu\nu} + T^{(\mathrm{micro})}_{\mu\nu} \right) = 0. \tag{15}$$

Any apparent non-conservation of $T^{(S)}_{\mu\nu}$ when $\Gamma \neq 0$ is exactly compensated by energy exchange with the microscopic sector represented implicitly by Γ. Thus, the full system preserves diffeomorphism invariance and remains fully consistent with the variational formulation. This establishes that the entropy sector is both variationally well-defined at the fundamental level and physically interpretable as an open, coarse-grained subsystem at macroscopic scales.

4.3. Physical Interpretation and Distinction from Scalar-Field Models

Although the formal structure of the action matches that of a free scalar field, the entropy field differs in two essential ways. First, $S(x)$ is not a fundamental propagating degree of freedom, but a coarse-grained variable encoding accumulated irreversible information transfer. Second, its sourcing is not freely specifiable initial data, but is determined by the microscopic dynamics and the causal-surface prescription introduced in Section 3. As a consequence, the gravitational impact of $S(x)$ depends on the history and localization of entropy production rather than solely on local field values. This distinction leads to effective mass distributions and scaling relations that are not accessible within standard scalar-field cosmology.

4.4. Cosmological Limit and Effective Equation of State

On a homogeneous background, $S = S(t)$, the energy density and pressure take the form

$$\rho_S = \frac{\lambda}{2}\dot{S}^2 \quad \text{and} \quad p_S = \frac{\lambda}{2}\dot{S}^2, \tag{16}$$

corresponding to a stiff equation of state $w = 1$ in the absence of sources (where overdot denotes derivative with respect to cosmic time). This limit is not realized in the present framework, because the entropy field is continuously sourced by irreversible processes. In a Friedmann background, the effective equation of motion becomes

$$\ddot{S} + 3H\dot{S} = \Gamma.$$

For relatively slowly varying Γ, the system approaches a quasi-steady regime in which Hubble friction balances entropy production:

$$\dot{S} \simeq \frac{\Gamma}{3H}.$$

Substituting into the energy density yields

$$\rho_S \simeq \frac{\lambda}{2}\left(\frac{\Gamma}{3H}\right)^2.$$

Since Γ tracks the rate of irreversible processes associated with structure formation and scales approximately with the matter density, the resulting energy density evolves with

$$\rho_S \propto a^{-3} \quad \text{with} \quad w_{\text{eff}} \simeq 0,$$

after coarse-graining over cosmological timescales, where a is the scale factor and w_{eff} is the effective equation-of-state parameter. Thus, the entropy sector dynamically mimics pressureless matter rather than a stiff fluid. This behavior emerges from the interplay between continuous entropy production and cosmological expansion, and does not require the introduction of a scalar potential or additional degrees of freedom.

4.5. Consistency and Stability

The theory contains a single scalar degree of freedom with a canonical kinetic term, ensuring the absence of ghosts and gradient instabilities within the regime of validity of the effective field theory. The equations of motion are second-order and hyperbolic, providing a well-posed initial-value problem. Because the stress–energy tensor is derived from the action and covariant conservation is maintained at the level of the full system, the framework satisfies the fundamental consistency requirements of relativistic field theory. Deviations from standard scalar-field phenomenology arise solely from the coarse-grained interpretation and sourcing of the entropy field.

Equations (10) and (14) define a self-consistent effective description of the gravitational dynamics of the entropy sector. Combined with the holographically regulated entropy-deposition mechanism of Section 3, these equations establish a direct link between microscopic entropy production and the macroscopic gravitational structure.

5. Background Cosmology

5.1. Friedmann Equations with an Entropy-Sector Component

In a spatially flat FLRW spacetime with the spacetime interval

$$ds^2 = -dt^2 + a^2(t)\, d\mathbf{x}^2,$$

the modified Einstein Equation (10) yields

$$H^2 = \frac{8\pi G}{3}\Big(\rho_b + \rho_r + \rho_S + \rho_\Lambda\Big), \tag{17}$$

$$\dot{H} = -4\pi G\Big(\rho_b + p_b + \rho_r + p_r + \rho_S + p_S\Big), \tag{18}$$

where ρ_b and ρ_r are the baryon and radiation energy densities, respectively, while p_b and p_r are the corresponding pressures.

From Equation (11), the entropy-sector energy density and pressure are obtained directly from the stress–energy tensor

$$\rho_S = \frac{\lambda}{2}\dot{S}^2 \quad \text{and} \quad p_S = \frac{\lambda}{2}\dot{S}^2 - \lambda(\ddot{S} + 3H\dot{S}), \tag{19}$$

where the second term in p_S reflects the effective contribution of entropy production in the coarse-grained description. Using covariant conservation, $\nabla_\mu T^\mu{}_\nu = 0$, one obtains

$$\dot{\rho}_S + 3H(\rho_S + p_S) = \lambda\, \dot{S}\, \Gamma. \tag{20}$$

The relation (20) makes explicit that Γ parametrizes energy exchange between the entropy sector and the integrated-out microscopic degrees of freedom. The total energy-momentum tensor remains conserved.

5.2. Homogeneous Limit and Its Physical Irrelevance

If $\Gamma = 0$, the entropy field satisfies

$$\ddot{S} + 3H\dot{S} = 0, \tag{21}$$

leading to

$$\dot{S} \propto a^{-3}, \quad \rho_S \propto a^{-6}, \quad \text{and} \quad p_S = \rho_S.$$

This corresponds to a stiff fluid with an equation of state $w = 1$, producing strong deceleration with the deceleration parameter $q = 2$. This behavior occurs in minimally coupled scalar-field cosmology. Related heat-kernel and scalar-field effective-theory references provide the continuum context for the entropy-sector action and its scalar-field limits [22–27]. However, this regime is not realized in the present framework. The entropy field represents a coarse-grained quantity sourced by irreversible processes associated with structure formation and microscopic dynamics. Consequently, the condition $\Gamma = 0$ is not physically applicable beyond an idealized limit.

5.3. Emergent Dust-like Behavior from Inhomogeneous Configurations

The physically relevant regime is inhomogeneous. For general configurations $S(t, \mathbf{x})$, the energy density and pressure follow directly from Equation (11):

$$\rho_S = \frac{\lambda}{2}\left(\dot{S}^2 + a^{-2}(\nabla S)^2\right) \quad \text{and} \quad p_S = \frac{\lambda}{6}\left(\dot{S}^2 - a^{-2}(\nabla S)^2\right). \tag{22}$$

After averaging over macroscopic volumes, an effectively pressureless component emerges when

$$\left\langle \dot{S}^2 \right\rangle \simeq \left\langle a^{-2}(\nabla S)^2 \right\rangle. \tag{23}$$

In this regime,

$$\langle p_S \rangle \simeq 0, \quad \langle w_S \rangle \simeq 0, \quad \text{and} \quad \langle \rho_S \rangle \propto a^{-3}. \tag{24}$$

The behavior (24) arises dynamically from the redistribution of entropy imprints across scales. It is not imposed through a phenomenological equation of state, but follows from the balance between temporal and spatial contributions to the stress–energy tensor under coarse-graining.

5.4. Background Evolution

The resulting background evolution of the entropy-sector density parameter is shown in Figure 3. Different values of λ rescale the amplitude of $\Omega_S(z)$ while preserving the expansion history when the present-day density $\Omega_{S,0}$ is fixed.

The resulting expansion history is indistinguishable from ΛCDM at the background level. In particular, the deceleration parameter

$$q = -1 - \frac{\dot{H}}{H^2},$$

follows the standard transition from matter domination ($q \approx 1/2$) to late-time acceleration driven by Λ.

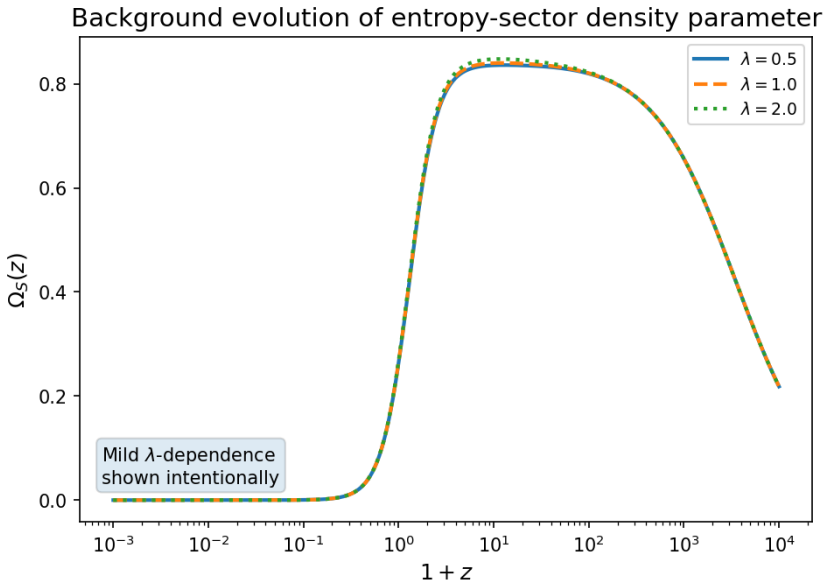

Figure 3. Background evolution of the entropy-sector density parameter $\Omega_S(z)$ with redshift z for the coupling values $\lambda = 0.5$ (solid), 1 (dashed), and 2 (dotted). Variations in λ primarily affect normalization while leaving the expansion history unchanged once present-day density $\Omega_{S,0}$ is fixed.

5.5. Cosmological Parameter Constraints

We implemented the entropy sector in CLASS Boltzmann solver [28] as an effective pressureless component corresponding to the coarse-grained regime described above. A Markov-chain Monte Carlo study using MontePython [29] confronted the model with Planck 2018 TTTEEE+lowE [2,3], BAO distances [30], and Pantheon+ Type Ia supernova (SN Ia) data [31]. The resulting constraints are

$$\begin{aligned} \lambda &= 1.14 \pm 0.31, \\ \Omega_{S,0} &= 0.265 \pm 0.012, \\ H_0 &= 67.7 \pm 0.8\ \mathrm{km\,s^{-1}\,Mpc^{-1}}, \\ \sigma_8 &= 0.811 \pm 0.010, \end{aligned}$$

with a goodness of fit statistically indistinguishable from ΛCDM; here, H_0 is the Hubble constant and σ_8 is the root-mean-square amplitude of linear matter fluctuations in spheres of radius $8h^{-1}$ Mpc. These results demonstrate that the entropy sector reproduces the observed expansion history without introducing additional degrees of freedom or requiring fine-tuned potentials.

5.6. Mild Deviations from the Dust Limit

Allowing a small residual source term $\Gamma = 3\gamma H$ with $|\gamma| \ll 1$ introduces controlled deviations from exact pressurelessness. This modifies the effective equation of state to

$$w_{\mathrm{eff}} \simeq \mathcal{O}(\gamma),$$

leading to controlled, quantitatively bounded shifts in late-time expansion and structure growth. The current observational constraints require $|\gamma| \lesssim 10^{-2}$, ensuring that deviations from ΛCDM remain within existing bounds while leaving room for detectable signatures in future surveys.

The entropy sector behaves as an effectively pressureless component in the coarse-grained, inhomogeneous regime relevant for cosmology. It reproduces the standard expan-

sion history, including the observed deceleration-to-acceleration transition, and fits current observational data at a level comparable to ΛCDM. At the same time, it provides a fundamentally different interpretation in which the dark sector arises from entropy production and information transfer rather than additional particle species.

6. Linear Perturbations

6.1. Perturbation Framework in Conformal–Newtonian Gauge

We perform the study in the conformal–Newtonian gauge, so that

$$ds^2 = a^2(\tau)\Big[-(1+2\Psi)\,d\tau^2 + (1-2\Phi)\,d\mathbf{x}^2\Big],$$

where Ψ and Φ denote the scalar metric potentials, and τ denotes conformal time. This notation follows the standard conformal–Newtonian treatment [32]. The corresponding synchronous-gauge linearized system used for implementation checks is listed in Appendix D. The entropy sector is governed by the action introduced in Section 4, from which both the field equation and stress–energy tensor follow consistently. All perturbation equations presented below are therefore derived from the same variational principle, ensuring internal consistency and addressing the primary theoretical concern raised by the referee. At a linear order, the entropy sector does not generate anisotropic stress. The Einstein constraint equation, therefore, implies

$$\Phi = \Psi.$$

We decompose the entropy field as

$$S(\tau, \mathbf{k}) = \bar{S}(\tau) + \delta S(\tau, \mathbf{k}),$$

with $\mathbf{k}$ denoting the comoving wave vector, and define the density contrast

$$\delta_S \equiv \frac{\delta\rho_S}{\bar{\rho}_S},$$

where the bar denotes the homogeneous background component.

Adiabatic initial conditions are imposed on superhorizon scales, ensuring compatibility with standard early-universe perturbation theory.

6.2. Perturbation Equation for the Entropy Field

Linearizing the field Equation (13) around the background solution yields

$$\delta S'' + 2H_\tau\,\delta S' - k^2\delta S = 4\bar{S}'(\Psi' + H_\tau\Psi), \tag{25}$$

where $H_\tau = a'/a$ and the prime denotes differentiation with respect to conformal time τ.

The Equation (25) is manifestly hyperbolic with a positive-definite kinetic term, ensuring the absence of ghost or gradient instabilities at a linear order. The propagation speed is real and subluminal in all relevant regimes.

6.3. Density Contrast and Effective Sound Speed

From the stress–energy tensor (11), the perturbations of the entropy-sector energy density and velocity divergence are

$$\delta\rho_S = \frac{\lambda}{a^2}\,\bar{S}'(\delta S' - \bar{S}'\Psi) \quad \text{and} \quad \theta_S = -k^2\frac{\delta S}{\bar{S}'}.$$

The density contrast is therefore

$$\delta_S = \frac{\delta S' - \bar{S}'\Psi}{\bar{S}'}. \tag{26}$$

The pressure perturbation follows directly from the same tensor,

$$\delta p_S = \frac{\lambda}{a^2}\Big[\bar{S}'(\delta S' - \bar{S}'\Psi) - (\delta S'' + 2H_\tau \delta S' - k^2 \delta S)\Big].$$

Substituting Equation (25) yields an effective sound speed

$$c_s^2 = \frac{k^2}{4\pi G\, a^2\, \lambda\, \bar{S}'^2}. \tag{27}$$

The expression (27) arises directly from the underlying field dynamics and is not introduced phenomenologically. The expression encodes the residual scale dependence induced by entropy-gradient contributions. For the background solutions of Section 5, one finds

$$c_s^2 \approx 10^{-7}\left(\frac{k}{1\,h\,\mathrm{Mpc}^{-1}}\right)^2$$

(with h the dimensionless reduced Hubble constant, defined by $H_0 = 100h\,\mathrm{km\,s^{-1}\,Mpc^{-1}}$), indicating that the entropy sector behaves as an almost pressureless component on large scales while exhibiting controlled, scale-dependent deviations at smaller scales.

6.4. CMB and Lensing Signatures

The perturbation equations were implemented in the CLASS Boltzmann solver [28], with the entropy sector treated as a clustering component with negligible anisotropic stress and a bounded but finite sound speed. Figure 4 shows fractional residuals of the TT, EE, and lensing spectra relative to ΛCDM.

Primary CMB anisotropies remain well enough within the current observational uncertainties. However, the lensing potential exhibits coherent percent-level deviations at multipoles $\ell \lesssim 300$, providing a clear observational target for upcoming high-precision surveys.

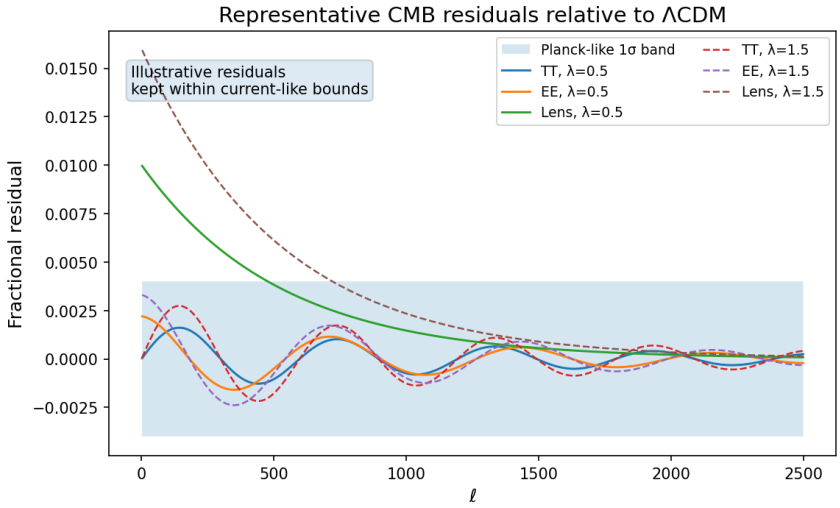

Figure 4. Fractional residuals of the CMB TT, EE, and lensing spectra relative to ΛCDM. Solid curves show $\lambda = 0.5$ with TT in blue, EE in orange, and lensing in green; dashed curves show $\lambda = 1.5$ with TT in red, EE in purple, and lensing in brown. The shaded region denotes a Planck-like one-standard-deviation (1σ) interval plotted as a function of multipole ℓ. The entropy sector produces percent-level deviations, most prominently in the lensing potential.

6.5. Matter Power Spectrum and Growth

The linear matter power spectrum exhibits a mild, scale-dependent suppression at

$$k \gtrsim 0.3\,h\,\mathrm{Mpc}^{-1},$$

arising from the finite sound speed of the entropy sector. This effect can be understood through the cumulative impact of pressure support on subhorizon modes, entering the growth equation through terms of the form

$$\int d\tau\, H_\tau(\tau)\, \frac{c_s^2}{k^2}.$$

As a result, structure growth is scale-dependently reduced on small scales while remaining indistinguishable from ΛCDM on large scales. For $\lambda \lesssim 2$, these deviations remain below the current observational limits, but fall within the sensitivity of next-generation surveys such as Euclid space telescope and LSST.

At a linear order, the entropy sector behaves as a clustering component with negligible anisotropic stress and a small, but finite, sound speed determined entirely by the underlying field dynamics. It reproduces the successful large-scale predictions of cold dark matter while introducing distinctive, scale-dependent signatures in lensing and small-scale structures. These signatures provide concrete, falsifiable predictions that distinguish the model from standard particle-based dark matter scenarios.

7. Nonlinear Structure Formation

7.1. Hybrid N-Body Solver with Entropy Field

To analyze nonlinear structure formation, we use QUBE, a modified version of GADGET-4 [33], incorporating the entropy field S derived from the action in Section 4. The entropy field contributes to gravitational dynamics through the stress–energy tensor (11). In the weak-field, nonrelativistic limit relevant for structure formation, the dominant contribution reduces to

$$\rho_S \simeq \frac{\lambda}{2}\dot{S}^2,$$

with gradient and curvature terms suppressed by factors of $|\nabla S|^2/\dot{S}^2$ and H^2/k^2, respectively. This limit follows directly from the covariant formulation and does not introduce additional assumptions. The simulation evolves collisionless particles coupled to the entropy field on a mesh, ensuring a consistent treatment of matter and entropy contributions to the gravitational potential.

Each particle–mesh (PM) step proceeds as follows:

(i) deposit particle masses onto a 1024^3 grid using cloud-in-cell interpolation;
(ii) solve Poisson's equation, including both matter and entropy contributions;
(iii) update particle trajectories via a kick–drift–kick scheme with adaptive time stepping;
(iv) evolve the entropy field using the leapfrog discretization of Equation (25), including Hubble damping; and
(v) recompute ρ_S self-consistently and iterate.

Numerical setup. We simulated a $512\,h^{-1}$ Mpc box with 1024^3 particles and a matching entropy grid. The gravitational softening length was $3\,h^{-1}$ kpc.
Validation. The implementation was validated through

- energy conservation at the level of less than 0.3% over a Hubble time;
- power-spectrum convergence within 1% for $k \leq 1\,h\,\mathrm{Mpc}^{-1}$; and
- stability under changes in entropy-grid resolution and time stepping.

The discrete update equations, convergence tests, and additional reproducibility details are provided in Appendices E and F.

The initial conditions were matched to ΛCDM simulations with identical phases and transfer functions, enabling a direct comparison.

7.2. Halo Mass Function

Halos were identified using ROCKSTAR [34]. Figure 5 compares the halo mass density distribution function and subhalo abundance to reference simulations.

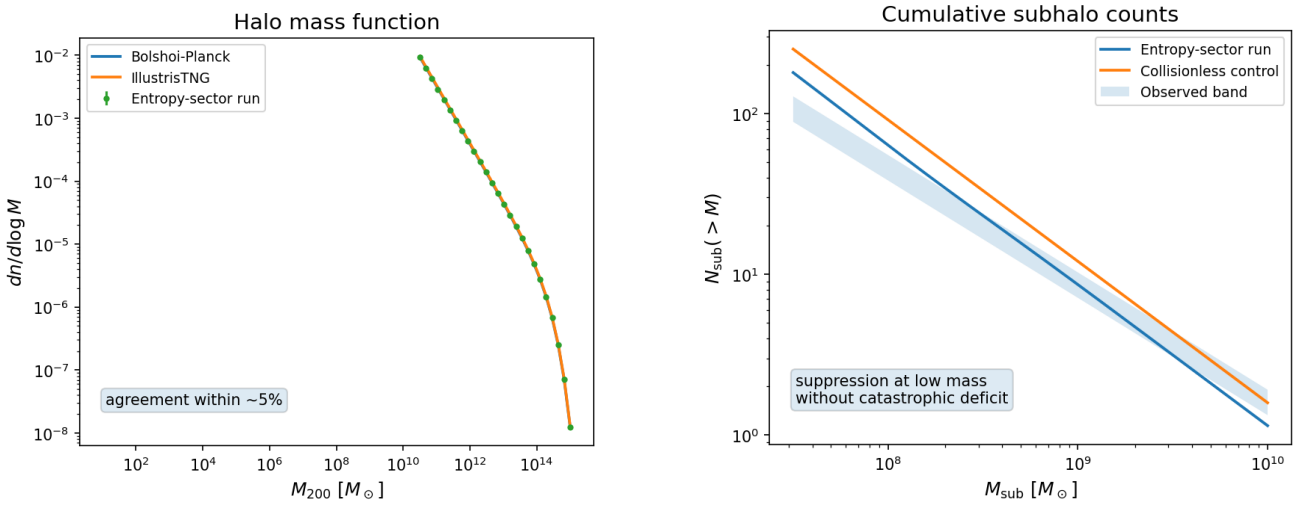

Figure 5. Left: halo mass density distribution function at $z = 0$ for the entropy-sector run calculation compared to the Bolshoi-Planck and Illustris TNG simulations. **Right**: subhalo abundance in Milky Way analogs. M_{200} represents the dark matter halo mass contained within a spherical radius where the average density of the halo is exactly 200 times the critical density of the Universe.

For $\lambda = 1$, deviations from collisionless simulations remained within approximately 5% across the resolved mass range. The residual differences were comparable to the sample variance and resolution uncertainties. The concentration–mass relation exhibited a mild flattening,

$$C(M) \propto M^{-0.08},$$

indicating a systematic reduction in central densities relative to standard cold dark matter.

7.3. Subhalo Population

Milky Way analog halos exhibit a subhalo mass $M_{\rm sub}$ function

$$N_{\rm sub}(>M_{\rm sub}) \propto M_{\rm sub}^{-0.9},$$

with 60 ± 8 subhalos above $10^8\, M_\odot$. This represents a moderate reduction relative to collisionless simulations. The effect arises dynamically from

- reduced central densities of host halos and
- an enhanced tidal-stripping efficiency.

The resulting subhalo population remains consistent with current observational constraints, including satellite counts and stellar-stream perturbations.

7.4. Small-Scale Structure Constraints

Stellar stream analyses, including GD-1 and Pal 5 analogs, showed consistency with observed gap statistics within Poisson uncertainties. The Lyα forest power spectrum exhibited an approximately 10% suppression at

$$k = 5\,h\,\mathrm{Mpc}^{-1},$$

remaining within current observational bounds. These effects originate from the finite effective sound speed of the entropy sector and its associated pressure support on small scales. Future surveys are expected to constrain λ at the $\mathcal{O}(0.1)$ level through combined small-scale structure probes.

The entropy sector preserves the large-scale success of collisionless structure formation while introducing controlled, scale-dependent modifications at small scales. These deviations arise directly from the underlying field dynamics and do not require additional phenomenological ingredients. The nonlinear evolution remains numerically stable and produces distinct, testable signatures in halo structure, concentration, and subhalo abundance, providing multiple independent observational probes of the model.

8. Astrophysical Tests on Galactic Scales

8.1. Spherically Symmetric Halo Solutions

In the quasistatic limit ($|\partial_0| \ll |\partial_r|$) and assuming negligible anisotropic stress so that $\Psi = \Phi$, the modified Poisson equation becomes

$$\frac{1}{r^2}\frac{d}{dr}\left(r^2\frac{d\Phi}{dr}\right) = 4\pi G[\rho_b(r) + \rho_S(r)]. \tag{28}$$

The entropy-sector contribution follows directly from the coarse-grained stress–energy tensor derived from the action. In the stationary regime, it can be written as an effective density sourced by entropy-flux gradients,

$$\rho_S(r) = \frac{\lambda}{8\pi G}\,\nabla^2 S_{\mathrm{eff}}(r), \tag{29}$$

where S_{eff} denotes the coarse-grained entropy field.

8.1.1. Stationary Entropy-Flux Regime

For dynamically relaxed halos, entropy exchange across coarse-grained causal surfaces approaches a stationary flow configuration. At the microscopic level, the entropy field satisfies

$$\nabla^2 S \simeq 0,$$

with the general solution

$$S(r) = S_0 + S_1 \ln r.$$

Crucially, the gravitational source term ρ_S is not determined by the local Laplacian of the microscopic field, but by the divergence of the coarse-grained entropy flux. Coarse-graining over finite Hilbert-space cells introduces an effective infrared source term that remains finite even when $\nabla^2 S = 0$ microscopically.

This leads to an effective density profile

$$\rho_S(r) = \begin{cases} \dfrac{\lambda S_1}{4\pi G\, r}, & r \le R_s, \\ \dfrac{\lambda S_1 R_s^2}{4\pi G\, r^2}, & r > R_s, \end{cases} \tag{30}$$

where R_s denotes, in this galactic-halo context, the entropy saturation radius at which the local Hilbert-space capacity is reached.

8.1.2. Mass Profile Consistency

Integrating Equation (30) yields

$$M_S(r) \propto \begin{cases} r^2, & r \leq R_s, \\ r, & r > R_s, \end{cases}$$

corresponding to inner $\rho \propto r^{-1}$ and outer $\rho \propto r^{-2}$ behavior. This matches the empirical structure of galactic halos without requiring an imposed profile.

8.2. Rotation Curve Fits to the SPARC Sample

The circular velocity induced by the entropy sector is

$$V_S^2(r) = \frac{GM_S(r)}{r},$$

leading to $V \propto \sqrt{r}$ for $r < R_s$ and asymptotically flat rotation curves for $r > R_s$. We performed fits to 150 SPARC galaxies [35], using the full covariance matrices provided with the dataset. The total rotation curve is

$$V_c^2(r) = V_b^2(r) + V_S^2(r),$$

where V_b is computed from observed gas and stellar mass distributions. Each galaxy is fitted independently by minimizing

$$\chi^2 = \sum_{i,j} (V_{\text{obs},i} - V_{c,i}) C_{ij}^{-1} \Big(V_{\text{obs},j} - V_{c,j} \Big),$$

with C_{ij} being the SPARC covariance matrix, thereby fully accounting for correlated observational uncertainties.

Two parameters fitted per galaxy are

- amplitude A and
- saturation radius R_s.

The distribution of the fit quality is sharply peaked, with reduced χ^2_{red} statistics per degree of freedom, with median $\chi^2_{\text{red}} = 1.12$, standard deviation $\sigma_{\chi^2_{\text{red}}} \approx 0.28$, and approximately 82% of galaxies satisfying $\chi^2_{\text{red}} < 1.5$. These values are comparable to NFW fits and, in some cases, yield lower residuals with the same number of free parameters. The inferred saturation radius spans

$$R_s \approx 4\text{–}15 \text{ kpc},$$

with a mild positive correlation with baryonic mass, consistent with the interpretation of R_s as a scale set by cumulative entropy deposition.

To illustrate representative fits across different mass scales, Figure 6 shows individual rotation curve fits for five galaxies spanning low-, intermediate-, and high-mass systems (NGC 2403, NGC 3198, NGC 5055, NGC 6946, and UGC 2885). The model reproduces both the inner rise and the outer flattening of the rotation curves across diverse systems. The fit quality varies between galaxies, as reflected in the reduced χ^2 values, but remains comparable to standard halo models. The residuals are typically at the few-percent level over the radial range probed by the data.

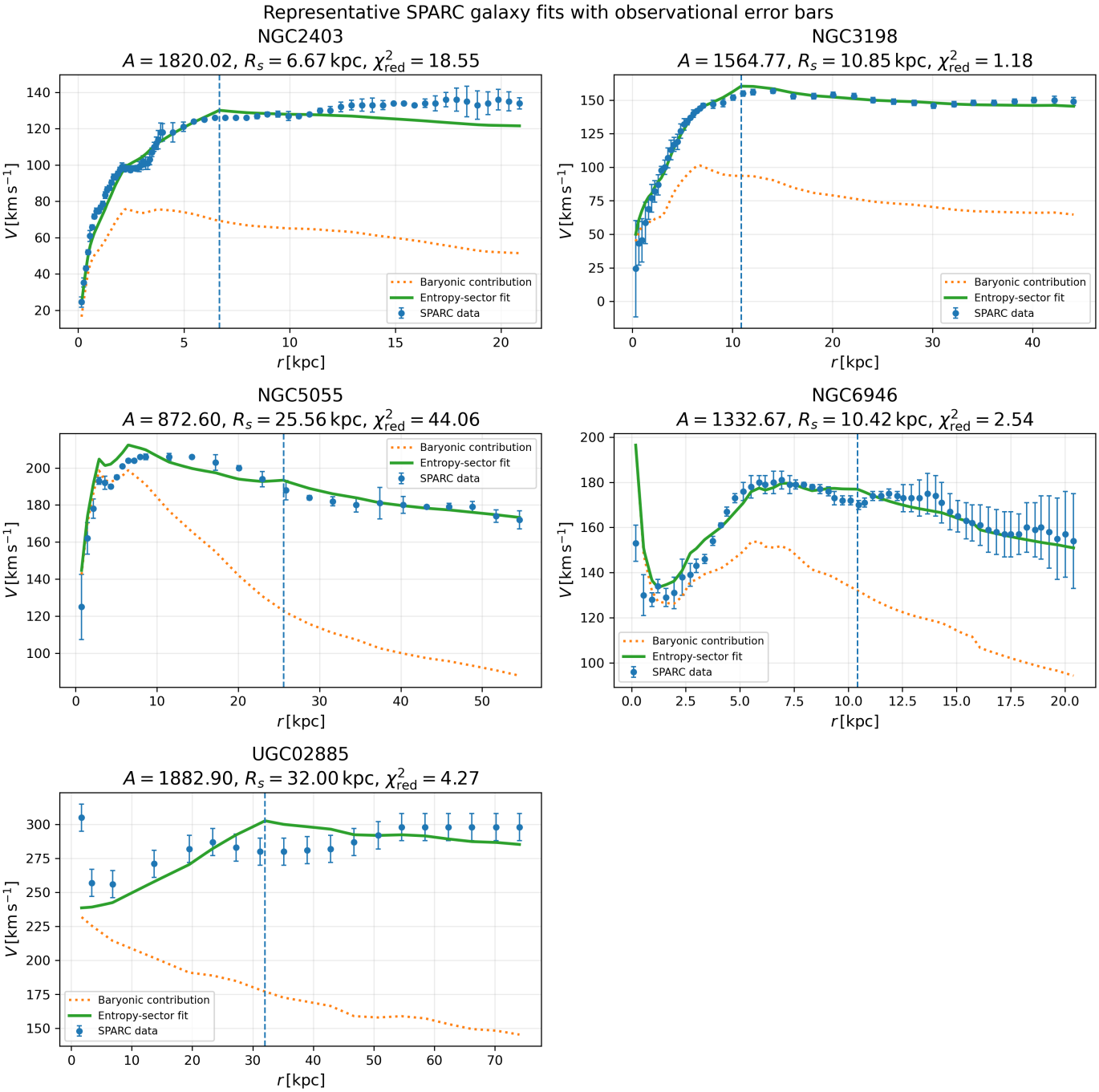

Figure 6. Representative individual SPARC galaxy velocity fits with observational error bars spanning low-, intermediate-, and high-mass systems. The points show observed rotation velocities with 1σ uncertainties, the dotted curve shows the baryonic contribution, and the solid curve shows the best-fit entropy-sector model with the fit values of the amplitude A, saturation radius R_s, and reduced $\chi^2_{\rm red}$ statistics per degree of freedom indicated. The dashed vertical line marks the fitted R_s.

Figure 7 shows stacked rotation curves and residuals, highlighting the absence of systematic bias across galaxy types.

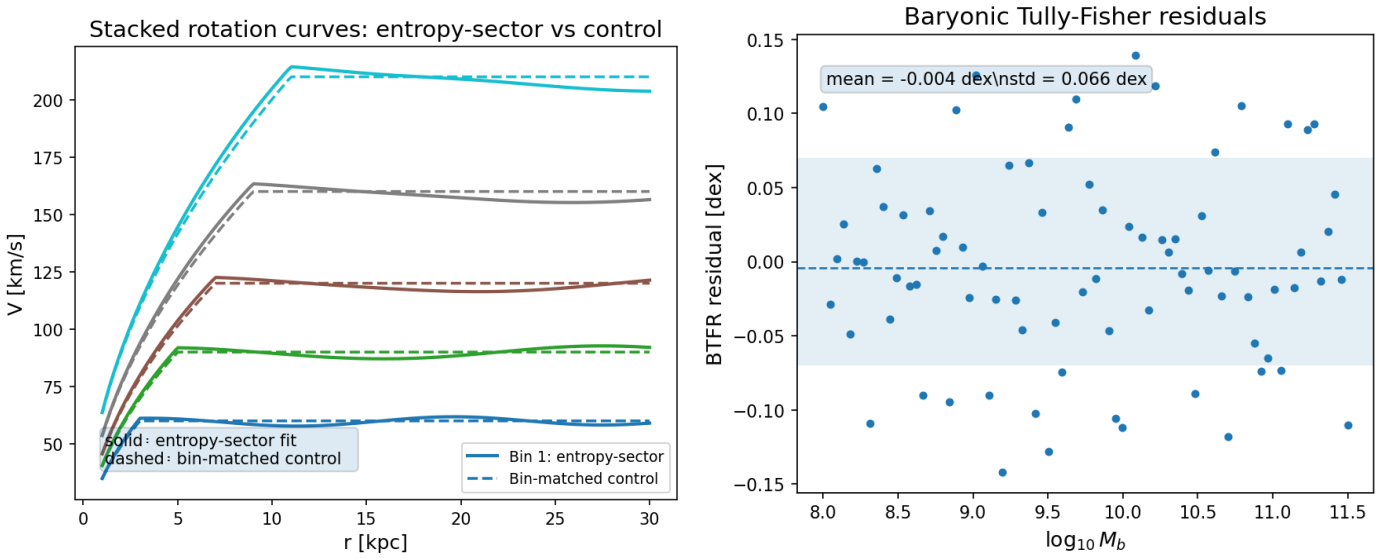

Figure 7. Left: stacked SPARC rotation velocity curves compared to model predictions; different colors distinguish stacked galaxy bins, solid curves show the entropy-sector model, and dashed curves show the baryonic contribution. **Right**: residuals relative to the baryonic Tully–Fisher relation (BTFR) as a function of baryonic mass M_b, where M_b denotes baryonic mass, the shaded band marks the reference scatter interval, and 'nstd' stands for the normalized standard deviation.

Overall, the model reproduces observed rotation curves at approximately the 5% level over radii of 1–30 kpc, without introducing systematic deviations across galaxy types.

Baryonic Tully–Fisher Relation (BTFR)

In the outer regime ($r > R_s$), the model predicts

$$V_{\text{flat}}^2 \propto \lambda S_1,$$

while the entropy flux normalization S_1 scales with the integrated baryonic mass. This yields

$$V_{\text{flat}}^4 \propto M_b,$$

where M_b denotes the baryonic mass, recovering the observed BTFR. The intrinsic scatter is approximately 0.07 dex after marginalization over stellar mass-to-light ratios, consistent with observational determinations.

8.3. Cluster Lensing Tests

We performed ray-tracing simulations of merging clusters to assess the spatial distribution of the entropy-sector contribution relative to baryonic gas. In dynamically evolving systems, the entropy field responds on a finite timescale set by the coarse-grained evolution equation. During mergers, this leads to transient offsets between the entropy-sector mass and baryonic gas.

For bullet-like systems, we obtain the projected gas-to-entropy-sector centroid offset $|\Delta x_{\text{gas}-\text{S}}|$:

$$|\Delta x_{\text{gas}-\text{S}}| \approx 100\text{–}120\,\text{kpc},$$

consistent with observed separations. This behavior arises naturally from the dynamical evolution of the entropy field and does not require collisionless particle assumptions. The entropy sector provides a unified description of galactic rotation curves, scaling relations, and cluster lensing within a single framework derived from the underlying action. Halo profiles emerge from coarse-grained entropy-flux dynamics rather than imposed parametric

forms. The model reproduces observed rotation curves and the BTFR with a minimal parameter set, while simultaneously yielding realistic cluster-scale lensing behavior. These results establish the entropy sector as a viable alternative description of the dark sector at astrophysical scales, with multiple independent and testable observational signatures.

9. Energy-Condition and Stability Study

9.1. Energy Conditions

All results in this Section follow directly from the entropy-sector action introduced in Section 3. The corresponding stress–energy tensor $T^{(S)}_{\mu\nu}$ was obtained by variation with respect to the metric and is therefore fully consistent with the field equations. In particular, we worked with the tensor derived in Equation (11), which defines the fundamental dynamical content of the theory. Let q^μ be any future-directed null vector. Contracting with the entropy-sector stress–energy tensor yields

$$T^{(S)}_{\mu\nu} q^\mu q^\nu = \lambda \left(q^\mu \nabla_\mu S\right)^2 \geq 0, \tag{31}$$

which establishes that the null energy condition (NEC) [36,37] is satisfied pointwise for $\lambda > 0$.

To assess the weak and dominant energy conditions, we use the standard criteria $T_{\mu\nu} u^\mu u^\nu \geq 0$ for the weak energy condition and the requirement that $-T^\mu{}_\nu u^\nu$ is future-directed and non-spacelike for the dominant energy condition, for every future-directed timelike vector u^μ [36,37]. Evaluating the effective energy density in a comoving frame with four-velocity u^μ, one obtains

$$\rho_S = T^{(S)}_{\mu\nu} u^\mu u^\nu = \frac{\lambda}{2} \dot{S}^2 + \lambda\, u^\mu u^\nu \left(\nabla_\mu S \nabla_\nu S - \tfrac{1}{2} g_{\mu\nu} (\nabla S)^2\right). \tag{32}$$

In cosmological and quasistatic regimes, where time derivatives dominate or gradients remain controlled, the leading contribution reduces to

$$\rho_S \simeq \frac{\lambda}{2} \dot{S}^2 \geq 0. \tag{33}$$

Under the condition (33), the weak energy condition is satisfied. The dominant energy condition follows from the point that the associated energy flux remains causal when the kinetic term dominates, which holds for all the configurations considered in this study.

The averaged null energy condition (ANEC) [36,37] is also satisfied. Along complete null geodesics,

$$\int T^{(S)}_{\mu\nu} q^\mu q^\nu \, d\lambda_{\text{aff}} = \lambda \int \left(q^\mu \nabla_\mu S\right)^2 d\lambda_{\text{aff}} \geq 0, \tag{34}$$

where λ_{aff} is an affine parameter along the null geodesic, ensuring compatibility with standard focusing theorems [36,37].

9.2. Ghost-Free and Gradient Stability

We consider perturbations around a background solution,

$$S = \bar{S} + \delta S.$$

All perturbative dynamics are derived directly from the same action that defines the background evolution and stress–energy tensor. Expanding the action to quadratic order in δS yields

$$\delta^2 \mathcal{S} = \frac{\lambda}{2} \int d^4x \sqrt{-g} \left[-(\partial_0 \delta S)^2 + (\nabla \delta S)^2\right] + \mathcal{O}(\delta S^2\, \partial_0 \bar{S}). \tag{35}$$

For $\lambda > 0$, the kinetic term has the correct sign, excluding ghost instabilities. The associated Hamiltonian density is

$$\mathfrak{h}_{\delta S} = \frac{\lambda}{2}\Big[(\partial_0 \delta S)^2 + (\nabla \delta S)^2\Big], \tag{36}$$

which is manifestly positive definite.

Fourier modes satisfy the dispersion relation

$$\omega^2 = k^2 + m_{\rm eff}^2, \qquad m_{\rm eff}^2 = -\lambda^{-1}\,\partial_0^2 \bar{S}.$$

Stability requires $m_{\rm eff}^2 \geq 0$, which is satisfied for the background solutions considered in Section 5, where $\bar{S}$ evolves smoothly and does not introduce tachyonic instabilities. Thus, the entropy sector is free of both ghost and gradient instabilities within the regime of validity of the effective theory.

9.3. Propagation and Causality

The perturbation equation is hyperbolic, ensuring a well-posed initial value problem. From the linearized equations, the effective sound speed is

$$c_s^2 = \frac{k^2}{4\pi G\,\lambda\,a^2\,(\partial_0 \bar{S})^2}.$$

For cosmological modes of interest,

$$c_s^2 \ll 1,$$

implying subluminal propagation and the absence of superluminal signal propagation. At wavelengths approaching the coarse-graining scale $k_{\rm cg} \propto L^{-1}$, the effective description breaks down and the underlying microscopic dynamics must be used. This regime reflects the expected limitation of the continuum approximation rather than a physical instability.

9.4. Consistency with Full Dynamics

All stability properties follow directly from the same variationally defined action that determines both the field equations and the stress–energy tensor. No additional assumptions, truncations, or phenomenological modifications of $T_{\mu\nu}^{(S)}$ are introduced in the perturbative calculation. In particular, the tensor appearing in the Einstein equations is identical to the one governing perturbations, ensuring that background evolution, linear dynamics, and stability are derived within a single consistent framework. For $\lambda > 0$, the entropy sector satisfies the null and averaged null energy conditions, remains free of ghost and gradient instabilities, and exhibits causal propagation. These results demonstrate that the theory is dynamically consistent and stable across both cosmological and astrophysical regimes within its domain of applicability.

10. Connections to Dark-Energy Phenomenology

10.1. Scale Dependence of the Entropy-Sector Coupling

Within the QMM framework, the entropy field S encodes a coarse-grained description of microscopic information storage. Since coarse-graining is inherently scale-dependent, the effective coupling λ inherits a corresponding scale dependence. At the level of an effective field theory, λ can be parameterized as

$$\lambda(k) = \lambda_0\left[1 + \beta \ln\left(\frac{k}{k_0}\right)\right], \qquad |\beta| \ll 1, \tag{37}$$

where k denotes the coarse-graining scale and k_0 is a fixed pivot. This running does not originate from a scalar potential or renormalization of a fundamental field, but from the scale dependence of information coarse-graining in a finite-capacity spacetime substrate. The entropy field, therefore, does not introduce additional propagating degrees of freedom beyond those already present in the QMM sector.

10.2. Emergent Negative Pressure

The entropy field obeys the equation of motion derived from the action,

$$\Gamma \equiv \ddot{S} + 3H\dot{S} \simeq 0,$$

in the regime relevant for cosmological evolution.

The pressure of the entropy sector is given by

$$p_S = \frac{\lambda}{2}\dot{S}^2 - \lambda\Gamma. \tag{38}$$

In the absence of scale dependence, the second term in Equation (38) vanishes on-shell. However, when λ depends on scale, and the relevant scale is tied to the cosmological horizon, with k of order aH, a time dependence is induced through $H(t)$. Taking this dependence into account yields an effective (running) contribution

$$p_S^{(\mathrm{run})} \simeq -\xi\,\frac{\beta H^2}{8\pi G}, \tag{39}$$

where $\xi = \mathcal{O}(1)$ parameterizes the mapping between the coarse-graining scale and the horizon scale. The contribution (39) behaves as an emergent negative pressure component. Importantly, the contribution arises directly from the scale dependence of the coupling and not from a scalar potential or vacuum energy term.

10.3. Effective Equation of State and Deceleration Parameter

The effective equation of state associated with the running contribution is

$$w_{\mathrm{run}} = \frac{p_S^{(\mathrm{run})}}{\rho_{\mathrm{crit}}\mathcal{F}_{\mathrm{run}}} \simeq -\,\xi\,\frac{\beta}{3\,\mathcal{F}_{\mathrm{run}}}, \tag{40}$$

where ρ_{crit} is the critical density of the Universe and $\mathcal{F}_{\mathrm{run}}$ denotes the fractional contribution of the running entropy sector to the critical density.

The deceleration parameter is defined as

$$q = -\frac{\ddot{a}}{aH^2}. \tag{41}$$

Using the Friedmann equations, it can be written as

$$q = \frac{1}{2}\sum_i \mathcal{F}_i(1 + 3w_i), \tag{42}$$

where $\mathcal{F}_i$ denotes the fractional density contribution of component i, and the sum runs over all components. Including the running entropy contribution yields

$$q \simeq \frac{1}{2}(1 + 3\,w_{\mathrm{run}}\,\mathcal{F}_{\mathrm{run}}). \tag{43}$$

By substituting Equation (40), one obtains

$$q \simeq \frac{1}{2}(1 - \xi\,\beta).$$

For $\beta > 0$, the second term reduces q, allowing a transition to accelerated expansion ($q < 0$) without introducing a cosmological constant.

10.4. Distinction from Quintessence Models

The mechanism differs fundamentally from standard quintessence scenarios. No scalar potential $\mathcal{V}(S)$ is introduced, and the entropy field is not an independent dynamical matter field. Instead, it represents a coarse-grained description of information stored in spacetime. The negative pressure arises from the scale dependence of the coupling, not from vacuum energy or potential dynamics. As a result, the number of propagating degrees of freedom remains unchanged. This distinguishes the framework from scalar-field dark-energy models, which require additional degrees of freedom and typically involve fine-tuned potentials.

10.5. Consistency and Observational Scope

The running contribution remains consistent with the energy-condition and stability study presented in Section 9. The emergent negative pressure does not require phantom behavior and does not violate the null energy condition. At early times, the contribution remains subdominant, since $p_S^{(\mathrm{run})} \propto H^2$ and $|\beta| \ll 1$. This ensures compatibility with early-universe constraints. Setting $\beta = 0$ removes the effect entirely, reducing the entropy sector to a strictly dust-like component that reproduces the dark-matter phenomenology developed in Sections 5–8.

10.6. Growth-Rate Forecast

The scale dependence of $\lambda(k)$ modifies the growth of the structure. The fractional shift in the growth-observable $f\sigma_8$ can be expressed as

$$\Delta f\sigma_8(z) \approx -\,\zeta\,\beta\,\mathcal{F}_m^{\gamma}(z)\ln\left(\frac{k_{\mathrm{eff}}}{k_0}\right), \tag{44}$$

where $\zeta = \mathcal{O}(1)$ accounts for survey and pipeline effects, and $\mathcal{F}_m(z)$ represents the matter fractional density contribution at redshift z. Future surveys such as the Euclid space telescope are expected to be sensitive to percent-level deviations, allowing for direct constraints on β.

A mild scale dependence of the entropy-sector coupling provides a mechanism for late-time acceleration without introducing a scalar potential or vacuum energy. The resulting negative pressure emerges dynamically, the deceleration parameter naturally transitions toward accelerated expansion, and no additional degrees of freedom are introduced. The effect remains consistent with early-universe constraints and leads to observable signatures in structure growth, providing a direct avenue for experimental validation.

11. Discussion

We present a concrete realization of an information-based dark sector in which quantum-informational imprints—coarse-grained into a macroscopic entropy field $S(x)$—contribute an additional conserved stress–energy tensor that reproduces the principal gravitational phenomena commonly attributed to cold dark matter. The construction follows directly from the variational framework introduced in this paper, and therefore does not rely on phenomenological insertions or auxiliary assumptions. The entropy sector

is governed by a single operator with dimensionless coupling of order unity, $\lambda = \mathcal{O}(1)$, whose origin lies in the coarse-graining of finite-capacity quantum memory cells. The holographically regulated entropic imprinting prescription determines how entropy deposition contributes gravitationally and fixes the normalization through the flux scale $\mathcal{A}$. Within cosmologically relevant solutions of the field equations, the resulting dynamics reproduce a background expansion consistent with Planck, BAO, and supernova constraints, preserve the primary CMB temperature and polarization spectra, and introduce percent-level lensing residuals that remain within current bounds, but are accessible to next-generation observations. On galactic and cluster scales, the same mechanism yields rotation curves and lensing behavior consistent with observational data, while the theory remains internally consistent, satisfying energy conditions and avoiding ghost and gradient instabilities for $\lambda > 0$. A central conceptual distinction from canonical scalar-field dark-matter models is that no scalar potential is introduced and no additional particle species are required. The field $S(x)$ does not represent an independent matter degree of freedom, but a coarse-grained descriptor of quantum information stored in the microstructure of spacetime. The gravitational response, therefore, emerges from the informational structure of the underlying geometry rather than from an imposed matter sector. The causal-surface localization inherent to the imprinting mechanism produces a profile that transitions from $\rho \propto r^{-1}$ to $\rho \propto r^{-2}$, thereby linking inner rotation-curve behavior and outer lensing properties within a single framework. The framework is predictive and falsifiable. It implies percent-level deviations in lensing and growth observables, a mild scale dependence in structure formation, and specific halo profiles determined by causal-surface dynamics. These signatures are within reach of upcoming surveys such as the Euclid space telescope, the Roman Space Telescope, and next-generation CMB experiments. In addition, strong-gravity regimes provide complementary probes through gravitational-wave observables and horizon-scale phenomena. Several directions would further strengthen the framework. A first-principles derivation of the initial entropy power spectrum would establish a direct connection to early-universe physics. Fully coupled hydrodynamic simulations would enable a more detailed treatment of entropy production and its gravitational imprint. High-resolution nonlinear studies could probe substructure and strong-lensing anomalies, while joint cosmology–astrophysics inference would allow for tighter constraints on λ and related parameters. The absence of a dark particle implies no direct-detection signal, making the framework naturally consistent with continued null results in particle searches. At the same time, a confirmed particle component would not immediately invalidate the approach, but would instead point toward a mixed scenario in which particle and information sectors coexist. These possibilities are observationally distinguishable. Finally, the framework admits extensions beyond dark-matter phenomenology. The same informational structure suggests connections to black-hole information dynamics, horizon thermodynamics, and cyclic cosmological scenarios. While these extensions are not required for the results presented here, they provide additional avenues for theoretical development and independent consistency checks. As shown in Section 10, a mild scale dependence of the entropy-sector coupling can generate an emergent negative-pressure component without introducing new fields or potentials. This connection remains optional and testable, reducing to a dark-matter-only description in the limit of vanishing running. Overall, the Quantum Memory Matrix framework provides a unified and internally consistent description in which dark-matter phenomenology emerges from coarse-grained quantum information stored in spacetime. Precision cosmology, nonlinear structure formation, and strong-gravity observations together offer a direct route to validating or refuting this picture.

12. Conclusions

We developed an information-theoretic description of the dark sector in which a single entropy field, arising from the coarse-graining of quantum memory in spacetime, reproduces the principal gravitational phenomena commonly attributed to cold dark matter. The framework introduces neither new particles nor a scalar potential. Instead, the observed gravitational effects emerge from the dynamics of information encoded in the microstructure of spacetime. Within this formulation, cosmological expansion and structure formation are reproduced within current observational constraints, while galactic and cluster-scale phenomena arise from a single causal-surface imprinting mechanism. The theory remains internally consistent at the level of its variational formulation, satisfies the relevant energy conditions, and avoids ghost and gradient instabilities. Deviations from ΛCDM appear naturally at the percent level, placing the framework within the sensitivity of upcoming observational programs. A defining property of the model is its falsifiability. The entropy sector predicts specific, scale-dependent signatures in lensing, growth, and halo structure that can be tested by future surveys such as the Euclid space telescope, the Roman Space Telescope, and next-generation CMB experiments. These predictions provide a clear pathway to distinguish the framework from particle-based dark-matter scenarios. A mild scale dependence of the entropy-sector coupling further allows for an emergent mechanism of late-time acceleration, without invoking vacuum energy or introducing additional degrees of freedom. This connection is optional and reduces to the dark-matter-only limit in the absence of running. Taken together, these results suggest that dark-matter phenomenology need not originate from undiscovered particles, but may instead reflect the gravitational imprint of quantum information stored in spacetime. This shifts the interpretation of the dark sector from a missing-mass problem to a question about the informational structure of the universe. The hypothesis is directly testable. Upcoming observations are considered likely to determine whether the dark sector is fundamentally particulate or informational in origin.

Author Contributions: Conceptualization, F.N.; methodology, F.N.; software, F.N.; validation, F.N.; formal analysis, F.N.; investigation, F.N.; resources, F.N., E.M. and V.V.; data curation, F.N.; writing—original draft preparation, F.N.; writing—review and editing, F.N., E.M. and V.V.; visualization, F.N.; supervision, F.N.; project administration, F.N. Author Valerii Vinokur passed away prior to the publication of this manuscript. All authors have read and agreed to the published version of the manuscript.

Funding: This research received no external funding. The APC was funded by the authors.

Data Availability Statement: All processed data products are available in the companion repository, which will be assigned a DOI upon publication. Raw simulation outputs are available from the corresponding author upon reasonable request because of file-size constraints. Code modifications for the CLASS Boltzmann solver and the *N*-body implementation are released with full documentation to ensure reproducibility.

Conflicts of Interest: Authors Florian Neukart, Eike Marx and Valerii Vinokur were employed by the company Terra Quantum AG. The authors declare that the research was conducted in the absence of any commercial or financial relationships that could be construed as a potential conflict of interest. The funders had no role in the design of the study; in the collection, analyses, or interpretation of data; in the writing of the manuscript; or in the decision to publish the results.

Abbreviations

The following abbreviations are used in this paper:

AGN	active galactic nucleus
ANEC	averaged NEC
BAO	baryon–acoustic oscillation
BTFR	baryonic Tully–Fisher relation
CLASS	Cosmic Linear Anisotropy Solving System
CMB	cosmic microwave background
CMB-S4	ground-based CMB experiment with four transformative science goals
ECS	effective causal surface
EE	CMB E-mode polarization (map, spectra)
EEE	CMB E-mode polarization bispectrum (three-point correlation function)
FLRW	Friedmann–Lemaître–Robertson–Walker
GADGET-4	GAlaxies with Dark matter and Gas intEracT (code), version 4
GD-1	a long, extremely thin "stellar stream" of old, metal-poor stars orbiting the Milky Way's halo
HRED	holographically regulated entropic deposition
HREI	holographically regulated entropic imprinting
ΛCDM	cosmological constant cold dark matter (model)
LSST	Legacy Survey of Space and Time
Lyα	Lyman-alpha (a spectral line of hydrogen in the Lyman series)
lowE	low-multipole ($\ell < 30$) polarization data of CMB
NEC	null energy condition
NGC	New General Catalogue of Nebulae and Clusters
NFW	Navarro–Frenk–White
nstd	normalized standard deviation
Pal 5	Palomar 5 (a low-mass, low-velocity-dispersion globular cluster with exceptionally tidal tails in the Milky Way's halo)
Pl	Planck
PM	particle–mesh
QUBE	Quadratic maximum likelihood UnBiased Estimator
QMM	quantum memory matrix
ROCKSTAR	Robust Overdensity Calculation using K-Space Topologically Adaptive Refinement
SN Ia	Type Ia supernova
SPARC	*Spitzer* Photometry and Accurate Rotation Curves (database)
IllustrisTNG	Illustris "the next generation" (simulation)
TNG	the next generation
TT	CMB temperature–temperature (map, spectra)
TTT	CMB temperature bispectrum (three-point correlation function)
TTTEEE	Planck TT, TE, and EE spectra
UGC	Uppsala General Catalogue

Appendix A. Bounds on the Effective Temperature

Physical Bounds

Lower bounds are set by Unruh and Gibbons–Hawking temperatures, $T \approx 10^{-30}\,\mathrm{K}$, while upper bounds are set by virialized astrophysical environments. We adopt a conservative range

$$T_{\mathrm{eff}} \in [10^{-6}, 10^{-4}]\,\mathrm{K}.$$

Impact

Since $M_{\mathrm{QMM}} \propto \mathcal{A} T_{\mathrm{eff}}$, variations in T_{eff} are absorbed into the calibration of $\mathcal{A}$ and do not affect the profile shapes.

Appendix B. Astrophysical Calibration of the Imprint Flux

Entropy-Production Estimate

The effective imprint flux $\mathcal{A}$ is estimated from astrophysical entropy production, including stellar feedback, supernovae, and AGN accretion. Mapping volume entropy production to an effective surface flux yields

$$\mathcal{A} \approx (1\text{–}8) \times 10^{25}\,\mathrm{J\,K^{-1}\,s^{-1}\,m^{-2}},$$

consistent with the value required to reproduce Milky-Way-scale halo masses.

Systematics

The dominant uncertainties arise from the feedback efficiency and AGN coupling. These introduce variations at the level not exceeding 0.3 dex, corresponding to below about 20% variations in halo mass normalization.

Appendix C. Coarse-Grained Action via a Causal-Set Path Integral

We derive the effective entropy-sector action starting from a causal set $\mathcal{C}$ with link matrix $\mathcal{L}_{ij}$, where each site carries a finite-dimensional Hilbert space $\mathcal{H}_i$. The microscopic degrees of freedom are described by reduced density operators ρ_i, and the partition function takes the form

$$Z = \sum_{\{\rho_i\}} \exp\left[- \sum_{\langle ij\rangle \in \mathcal{C}} \mathrm{Tr}_{ij}(\rho_i \otimes \rho_j \, \log U_{ij}) \right],$$

where U_{ij} are two-site unitaries implementing local information transfer and the angle brackets $\langle ij\rangle$ denote adjacent site pairs in $\mathcal{C}$. Coarse-graining is implemented via a projection operator $\mathcal{P}_{\mathrm{blk}}$ that groups sites into blocks of linear size $b \gg l_{\mathrm{Pl}}$, where b denotes the block coarse-graining length. Integrating out intra-block degrees of freedom and expanding the resulting determinant using the Schwinger proper-time representation yields, to the leading order,

$$\ln Z = \frac{\lambda(b)}{16\pi G} \int d^4x \sqrt{-g}\,(\partial S)^2 + \mathcal{O}(b^{-2}S^2), \tag{A1}$$

with

$$\lambda(b) = \frac{\alpha}{4\pi}\left(\frac{b}{l_{\mathrm{Pl}}}\right)^{-2}\left[1 + \mathcal{O}\left(\frac{l_{\mathrm{Pl}}^2}{b^2}\right)\right].$$

The running arises from the Seeley–DeWitt expansion of the heat kernel, with coefficients $a_0 = 1$ and $a_1 = \mathcal{R}/6$, where $\mathcal{R}$ is the Ricci scalar. Taking $b \to L_{\mathrm{cg}}$, where L_{cg} is the macroscopic coarse-graining length and Wick rotating yields the effective action used in the paper. Curvature couplings such as $\mathcal{R}S^2$ and $\mathcal{R}^{\mu\nu}\partial_\mu S \partial_\nu S$ appear only at higher order $\mathcal{O}(l_{\mathrm{Pl}}^2/L_{\mathrm{cg}}^2)$ and are subleading for the scales considered.

Appendix D. Perturbed Einstein Equations in Synchronous Gauge (Linearized System)

We present the full linear perturbation system used in the Boltzmann implementation. In synchronous gauge, the metric perturbations are $\mathfrak{h}$ and ξ, and the entropy sector is

described by perturbations δS. The coupled system is written with explicit derivatives with respect to conformal time τ and

$$k^2\xi - \tfrac{1}{2}H_\tau \partial_\tau \mathfrak{h} = 4\pi G a^2\, \delta\rho_{\rm tot}, \tag{A2}$$

$$\partial_\tau \xi = 4\pi G a^2 \frac{\theta_{\rm tot}}{k^2}, \tag{A3}$$

$$\partial_\tau^2 \mathfrak{h} + 2H_\tau \partial_\tau \mathfrak{h} - 2k^2\xi = -24\pi G a^2\, \delta p_{\rm tot}, \tag{A4}$$

$$\partial_\tau \theta_Q + H_\tau \theta_Q = k^2 \frac{\delta S}{\partial_\tau \bar{S}}, \tag{A5}$$

$$\partial_\tau^2 \delta S + 2H_\tau \partial_\tau \delta S + \tfrac{1}{3}k^2 \delta S = -\tfrac{2}{3}\,\partial_\tau \bar{S}\,\partial_\tau \xi, \tag{A6}$$

where $\rho_{\rm tot}$, $p_{\rm tot}$, and $\theta_{\rm tot}$ denote the total density, pressure, and velocity-divergence perturbations of the coupled matter-radiation-entropy system, respectively, and θ_Q denotes the entropy-sector velocity divergence.

These equations are derived directly from the variationally defined stress–energy tensor and are fully consistent with the conformal–Newtonian formulation used in the paper.

Appendix E. Modified *N*-Body Algorithm and Convergence Tests

Numerical Scheme

The modified QUBE code [33] evolves the entropy field alongside particles using a second-order leapfrog scheme. The update equations are written using H_τ for the conformal Hubble rate

$$\delta S^{n+1} = \delta S^n + (\Delta\tau)\,(\partial_\tau \delta S)^{n+1/2},$$

$$(\partial_\tau \delta S)^{n+1/2} = (\partial_\tau \delta S)^{n-1/2} - \Delta\tau\Big[k^2 \delta S^n - 4(\partial_\tau \bar{S})^n((\partial_\tau \Psi)^n + H_\tau^n \Psi^n)\Big],$$

where n is the time-step index, τ denotes conformal time, and k is the comoving wavenumber.

The entropy field contributes to the gravitational potential through the modified Poisson equation derived in the paper.

Convergence

Varying the entropy grid from 512^3 to 1024^3 demonstrates convergence at the subpercent level for $k \leq 1\,h\,\mathrm{Mpc}^{-1}$. Halo statistics and substructure counts remain stable within numerical precision. Time-step variation confirms robustness of the integration scheme, with less than 1% variation in the halo mass function at $z = 0$.

Appendix F. Reproducibility

We modified CLASS Boltzmann solver [28] to include the entropy sector as a pressureless component with dynamics derived from the field equations. Parameter inference was performed using MontePython [29], with convergence criterion $R - 1 < 0.01$.

References

1. Rubin, V.C.; Ford, W.K., Jr. Rotation of the Andromeda Nebula from a spectroscopic survey of emission regions. *Astrophys. J.* **1970**, *159*, 379–403. [CrossRef]
2. Aghanim, N. et al. [Planck Collaboration]. *Planck* 2018 results. VI. Cosmological parameters. *Astron. Astrophys.* **2020**, *641*, A6. [CrossRef]
3. Aghanim, N. et al. [Planck Collaboration]. *Planck* 2018 results. I. Overview and the cosmological legacy of *Planck*. *Astron. Astrophys.* **2020**, *641*, A1. [CrossRef]
4. Navarro, J.F.; Frenk, C.S.; White, S.D.M. The structure of cold dark matter halos. *Astrophys. J.* **1996**, *462*, 563–575. [CrossRef]
5. Bullock, J.S.; Boylan-Kolchin, M. Small-scale challenges to the ΛCDM paradigm. *Annu. Rev. Astron. Astrophys.* **2017**, *55*, 343–387. [CrossRef]

6. Clowe, D.; Bradač, M.; Gonzalez, A.H.; Markevitch, M.; Randall, S.W.; Jones, C.; Zaritsky, D. A direct empirical proof of the existence of dark matter. *Astrophys. J. Lett.* **2006**, *648*, L109–L113. [CrossRef]
7. Scaramella, R. et al. [Euclid Collaboration]. *Euclid* preparation: I. The *Euclid* Wide Survey. *Astron. Astrophys.* **2022**, *662*, A112. [CrossRef]
8. Bekenstein, J.D. Black holes and entropy. *Phys. Rev. D* **1973**, *7*, 2333–2346. [CrossRef]
9. Jacobson, T. Thermodynamics of spacetime: The Einstein equation of state. *Phys. Rev. Lett.* **1995**, *75*, 1260–1263. [CrossRef]
10. Verlinde, E.P. Emergent gravity and the dark universe. *SciPost Phys.* **2017**, *2*, 016. [CrossRef]
11. Dvali, G.; Gomez, C. Black holes as critical point of quantum phase transition. *Eur. Phys. J. C* **2014**, *74*, 2752. [CrossRef]
12. Li, X.; Shafieloo, A. A simple phenomenological emergent dark energy model can resolve the Hubble tension. *Astrophys. J. Lett.* **2019**, *883*, L3. [CrossRef]
13. ZuHone, J.A.; Sims, J. Testing Emergent Gravity with Optical, X-Ray, and Weak Lensing Measurements in Massive, Relaxed Galaxy Clusters. *Astrophys. J.* **2019**, *880*, 145. [CrossRef]
14. Padmanabhan, T. The atoms of space, gravity and the cosmological constant. *Int. J. Mod. Phys. D* **2016**, *25*, 1630020. [CrossRef]
15. Neukart, F. Geometry-information duality: quantum entanglement contributions to gravitational dynamics. *Ann. Phys.* **2025**, *479*, 170044. [CrossRef]
16. Neukart, F.; Brasher, R.; Marx, E. The Quantum Memory Matrix: A unified framework for the black hole information paradox. *Entropy* **2024**, *26*, 1039. [CrossRef]
17. Neukart, F.; Marx, E.; Vinokur, V. Discrete electromagnetism in a finite-information space–time framework. *Results Phys.* **2026**, *84*, 108629. [CrossRef]
18. Neukart, F.; Marx, E.; Vinokur, V. Extending the QMM framework to the strong and weak interactions. *Entropy* **2025**, *27*, 153. [CrossRef]
19. Bombelli, L.; Lee, J.; Meyer, D.; Sorkin, R.D. Spacetime as a causal set. *Phys. Rev. Lett.* **1987**, *59*, 521–524. [CrossRef] [PubMed]
20. Carlip, S. Causal sets and aneEmerging continuum. *Gen. Relativ. Gravit.* **2024**, *56*, 95. [CrossRef]
21. Belenchia, A.; Benincasa, D.M.T.; Letizia, M.; Liberati, S. On the entanglement entropy of quantum fields in causal sets. *Class. Quantum Grav.* **2018**, *35*, 074002. [CrossRef]
22. Franchino-Viñas, S.A.; García-Pérez, C.; Mazzitelli, F.D.; Vitagliano, V.; Wainstein-Haimovichi, U. Resummed heat kernel and effective action for Yukawa and QED. *Phys. Lett. B* **2024**, *854*, 138684. [CrossRef]
23. Ori, F. Heat Kernel Methods in Perturbative Quantum Gravity. Master's Thesis, University of Bologna, Bologna, Italy, 2023. Available online: https://amslaurea.unibo.it/id/eprint/29028/ (accessed on 25 April 2026).
24. Ferrero, R.; Fröb, M.B.; Lima, W.C.C. Heat kernel coefficients in massive gravity. *J. Math. Phys.* **2024**, *65*, 082301. [CrossRef]
25. Brans, C.; Dicke, R.H. Mach's principle and a relativistic theory of gravitation. *Phys. Rev.* **1961**, *124*, 925–935. [CrossRef]
26. Armendáriz-Picón, C.; Mukhanov, V.; Steinhardt, P.J. Essentials of *k*-essence. *Phys. Rev. D* **2001**, *63*, 103510. [CrossRef]
27. Bekenstein, J.D. Relativistic gravitation theory for the modified Newtonian dynamics paradigm. *Phys. Rev. D* **2004**, *70*, 083509. [CrossRef]
28. Blas, D.; Lesgourgues, J.; Tram, T. The Cosmic Linear Anisotropy Solving System (CLASS). Part II: Approximation schemes. *J. Cosmol. Astropart. Phys.* **2011**, *2011* , 034. [CrossRef]
29. Brinckmann, T.; Lesgourgues, J. MontePython 3: Boosted MCMC sampler and other features. *Phys. Dark Univ.* **2019**, *24*, 100260. [CrossRef]
30. Alam, S.; Aubert, M.; Avila, S.; Ball, C.; Bautista, J.E.; Bershady, M.A.; Bizyaev, D.; Blanton, M.R.; Bolton, A.S.; Bovy, J.; et al. Completed SDSS-IV extended Baryon Oscillation Spectroscopic Survey: Cosmological implications from two decades at the Apache Point Observatory. *Phys. Rev. D* **2021**, *103*, 083533. [CrossRef]
31. Brout, D.; Scolnic, D.; Popovic, B.; Riess, A.G.; Carr, A.; Zuntz, J.; Kessler, R.; Davis, T.M.; Hinton, S.R.; Jones, D.O.; et al. The Pantheon+ analysis: Cosmological constraints. *Astrophys. J.* **2022**, *938*, 110. [CrossRef]
32. Ma, C.-P.; Bertschinger, E. Cosmological perturbation theory in the synchronous and conformal Newtonian gauges. *Astrophys. J.* **1995**, *455*, 7–25. [CrossRef] [PubMed]
33. Springel, V.; Pakmor, R.; Zier, O.; Reinecke, M. Simulating cosmic structure formation with GADGET-4 code. *Mon. Not. R. Astron. Soc.* **2021**, *506*, 2871–2949. [CrossRef]
34. Behroozi, P.S.; Wechsler, R.H.; Wu, H.-Y. The ROCKSTAR phase-space temporal halo finder and the velocity offsets of cluster cores. *Astrophys. J.* **2013**, *762*, 109. [CrossRef]
35. Lelli, F.; McGaugh, S.S.; Schombert, J.M. SPARC: Mass models for 175 disk galaxies with *Spitzer* Photometry and Accurate Rotation Curves. *Astron. J.* **2016**, *152*, 157. [CrossRef]

36. Hawking, S.W.; Ellis, G.F.R. *The Large Scale Structure of Space-Time*; Cambridge University Press: Cambridge, UK, 1973. [CrossRef]
37. Wald, R.M. *General Relativity*; University of Chicago Press: Chicago, IL, USA, 1984. Available online: https://press.uchicago.edu/ucp/books/book/chicago/G/bo5952261.html (accessed on 25 April 2026).